Earth Planet. Sci. Lett. 690 (2026) 120123

Contents lists available at ScienceDirect

Earth and Planetary Science Letters

journal homepage: www.elsevier.com/locate/epsl

Mantle melting and magma ocean dynamics on Mercury impacted by sulfur in reduced mafic magmas

Xiaofeng Lu[a,b], Olivier Namur[c], Yongjiang Xu[a], Bernard Charlier[d], Yanhao Lin[a,*]

[a] Lin Earth and Planetary Laboratory, Center for High pressure Science and Technology Advanced Research, Beijing, 100193, China
[b] School of Earth Sciences and Resources, China University of Geosciences, Beijing, 100083, China
[c] Earth and Environmental Sciences, KU Leuven, 3001, Leuven, Belgium
[d] Department of Geology, University of Liège, 4000, Sart Tilman, Belgium

ARTICLE INFO

Editor: DR J BADRO

Keywords:
Sulfur
Melting temperature
Magma generation
Experimental petrology
Stratified mantle

ABSTRACT

Chemical data from the MESSENGER spacecraft reveal that Mercury's lavas are unusually sulfur-rich, suggesting highly reduced conditions during their formation. As a major volatile, sulfur profoundly affects the physical and chemical properties of silicate melts, potentially impacting key processes such as magma ocean crystallization and mantle melting. Here we conducted near-liquidus experiments (1650–2000 °C and 3–5 GPa) to quantify the effect of sulfur on phase relations in olivine- and orthopyroxene-saturated mafic compositions representative of Mercury's mantle. Our results show that elevated sulfur contents (up to 6 wt.% S) can depress the liquidus of Mercurian mantle by up to 200 °C. The liquidus depression of silicate melt is positively correlated with sulfur concentrations, negatively correlated with pressure, and compositionally-sensitive with a larger S-effect on higher Mg/Si melt. Using a newly developed parameterization for sulfur-bearing melting, we show that the mantle potential temperatures required to produce the volcanic provinces are lower than previously estimated. Furthermore, modeling of magma ocean cooling and crystallization dynamics indicates that sulfur-induced liquidus depression can extend solidification timescales by tens to hundreds to thousands of years, especially beneath an insulating graphite crust (>100 m). Using viscosity models, we find that sulfur also reduces the critical crystal size for settling, thus promoting fractional crystallization and formation of a chemically stratified mantle. These findings provide critical constraints on Mercury's interior structure and show that sulfur lowers the solidus and liquidus, enhances melt production, and helps to explain Mercury's fertile mantle, extensive crustal formation, and diverse surface lavas.

1. Introduction

Volatile components in magmas such as H_2O, CO_2, O, F, Cl, and S significantly affect their physicochemical properties, including melting temperature, crystallization sequence, and phase transitions (e.g. Almeev et al., 2007, 2012; Botcharnikov et al., 2008; Filiberto and Treiman, 2009; Filiberto et al., 2012; Lin et al., 2017, 2024; Médard and Grove, 2008; Sisson and Grove, 1993; Xu et al., 2026; Zhang and Dasgupta, 2026).

Data from the MESSENGER spacecraft revealed that Mercury's surface is notably enriched in sulfur, with concentrations ranging from 1.5 to 4 wt.% (Nittler et al., 2018), significantly exceeding those of other terrestrial planets. Mercury's surface is also characterized by Mg-rich and Al-, Ca- and Fe-poor lavas. In contrast, Mercury's bulk composition is iron-rich, attributed to the disproportionately large core (Hauck et al., 2013; Margot et al., 2018; Weider et al., 2014). The low iron and high sulfur contents in surface lava suggest a highly reduced Mercury (Cartier and Wood, 2019). Based on the surface S contents, Mercury's oxygen fugacity was estimated at IW-5.4 ± 0.4 (Namur et al., 2016a; IW = iron-wüstite buffer), although a broader range from IW-2 to IW-7 has been proposed (McCubbin et al., 2012; Zolotov et al., 2013).

Previous studies indicate that sulfide (S^{2-}) is the dominant sulfur species in silicate melts at highly reducing conditions relevant to Mercury (Jugo et al., 2010; Namur et al., 2016a). As oxygen fugacity (fO_2) decreases from IW-2 to IW-7, different sulfide species in the melt are observed: CaS becomes dominant with minor TiS and Na_2S at IW-2 to IW-4, and MgS emerges as the principal S-bearing species with minor CaS at $\leq$ IW-4 (Anzures et al., 2025, 2020). This suggests that S

---

[*] Corresponding author.
E-mail address: yanhao.lin@hpstar.ac.cn (Y. Lin).

https://doi.org/10.1016/j.epsl.2026.120123
Received 31 January 2026; Received in revised form 13 May 2026; Accepted 19 May 2026

preferentially bonds with Mg and Ca, potentially impacting the activities of MgO and CaO (a_{MgO} and a_{CaO}) in the silicate melts at reducing conditions. A reduction in a_{CaO} primarily influences the crystallization of lower-temperature phases (e.g. clinopyroxene and plagioclase; Anzures et al., 2020; Mouser et al., 2021), while a decrease in a_{MgO} significantly impacts higher-temperature crystallization by destabilizing olivine in favor of orthopyroxene (Anzures et al., 2025; Namur et al., 2016b; Saracino et al., 2025). At elevated S contents, it has also been shown that S bonds with Si in addition to Mg^{2+} and Ca^{2+}(Pommier et al., 2023), which affects a_{SiO_2}, underscoring the complex role of S in controlling melt structure and crystallization behavior.

Despite predictions that high sulfur concentrations in the reduced Mercurian magmas influence phase equilibria (Anzures et al., 2025, 2020; Namur et al., 2016b), the experimental data remain insufficient to quantitatively assess the role of sulfur in magma ocean solidification and subsequent mantle melting behavior. In this study, we conducted high-pressure (3 and 5 GPa) and high-temperature (1650–2000 °C) experiments on compositions representative of the bulk silicate composition of Mercury. These compositions were determined based on the bulk silicate fraction of enstatite chondrites (EH-EL chondrites; Lodders and Fegley, 1998; Y. Xu et al., 2024), with four different sulfur contents in the bulk starting compositions (0–7.3 wt.%; Table 1). The selected pressure range corresponds to conditions of an average mantle pressure (3 GPa) to the core-mantle boundary (CMB; 5 GPa). Our experimental results provide a quantitative framework for understanding sulfur-induced liquidus depression, and its role on enhancing partial melting of the mantle. We also investigate the role of sulfur on the dynamics of Mercury's magma ocean which we find substantial but still marginal compared to the role of a graphite primary crust (Mouser and Dygert, 2023; Peplowski et al., 2016; R. Xu et al., 2024).

2. Methods

2.1. Starting composition

The primitive mantle of Mercury is commonly thought to resemble the silicate portion of enstatite chondrites (EH-EL chondrites; Nittler et al., 2018; Y. Xu et al., 2024). We thus compiled the chemical compositions of EH-EL meteorites (Berthet et al., 2009; Jarosewich, 1990), excluding metallic iron and reducing the phosphorus content relative to the bulk EH-EL values due to its siderophile behavior at reduced conditions (Steenstra et al., 2020, 2018). Given that Si partitions into metallic melts under highly reduced conditions (Chabot et al., 2014; Kilburn and Wood, 1997), we prepared two silicate starting compositions: Mer10 and Mer20, representing 10 and 20% of the planet's bulk Si partitioned into the metallic core, respectively (Table 1). These values align with the most plausible interior structure and thermal models for Mercury (5.6 ± 3.1 wt.% Si; Goossens et al., 2022; Knibbe et al., 2021). The silicate compositions were mixed with FeS or Fe^0 in different proportions (Table 1) to achieve a range of sulfur contents (0–7.30 wt.% S in the bulk starting compositions). For sulfur-free compositions, pure Fe^0 was added as metal phase was required for post-run oxygen fugacity calculations.

The silicate compositions were produced using high-purity commercial oxides and phosphate powders (SiO_2, MgO, TiO_2, Al_2O_3, MnO, Cr_2O_3, $AlPO_4$) and synthetic silicates ($CaSiO_3$, Na_2SiO_3, $K_2Si_4O_9$,) prepared from oxides and carbonates. The reagents were homogenized in an agate mortar to ensure uniformity. In order to reduce the intrinsic oxygen fugacity (fO_2) of the sample, we added Si metal to the starting composition (Berthet et al., 2009; Cartier et al., 2014; Malavergne et al., 2014). In order to keep similar cation ratios in all experiments, we kept the Si/SiO_2 ratio constant (0.2; Namur et al., 2016a).

2.2. Experimental, analytical methods and oxygen fugacity

All experiments were conducted using a six-anvil cubic press (GY420, applying up to 6 × 14 MN force) at the Center for High Pressure Science and Technology Advanced Research (HPSTAR), in Beijing, following the assembly method and pressure calibration described in Wu et al. (2024) and Xu et al. (2026) (see additional details in Fig. S1). For all experiments we use a hand-machined graphite capsule with a 0.7 mm inner diameter, 1.6 mm outer diameter, ~1.8 mm length. The capsule was drilled along a length of ~0.8 mm in order to minimize the temperature gradient within the sample. The capsule was loaded with starting material and sealed with a graphite lid. Temperature was monitored using a $W_{97}Re_3$-$W_{75}Re_{25}$ (Type-D) thermocouple. Samples were pressurized to target pressure at room temperature before being heated to the desired temperature under constant pressure. Experimental conditions are provided in Table 2.

Experimental run products were embedded in epoxy and polished to 1 µm, then carbon-coated. Phase identification (Fig. 1) and quantitative analyses were conducted using a JEOL JXA-8230 electron microprobe at the Testing Center of the Shandong Bureau of the China Metallurgical Geology Bureau. Major and minor elements in all phases were analyzed at 15 kV accelerating voltage, with a 10 nA focused beam for silicate minerals, and 8–10 nA defocused beam (10 µm diameter) for silicate melt to minimize beam damage and alkali migration. We used a 20 nA focused beam for sulfide and metallic alloy phases. Primary calibrating standards included natural minerals and synthetic oxides for silicate (Si and Na, jadeite; Ti, rutile; Al, garnet; Fe, fayalite; Mg, forsterite; Ca, diopside; K, sanidine; Cr, chromite; Mn, rhodonite; P, apatite; S, pyrrhotite), natural sulfide minerals and pure metals for sulfide and metallic alloys. NAverage compositions and standard deviations of all phases are reported in Supplementary Dataset 1. For each experiment, mineral and silicate melt proportions were calculated using a multiple least-squares mass balance method. This approach determined the weight fraction of each phase by minimizing the compositional residuals between the nominal starting bulk composition (Table 1) the combined EPMA compositions of the coexisting phases (Table 2).

The intrinsic fO_2 of the samples were calculated using the

Table 1
Average composition of the silicate fraction of EH-EL meteorites and starting compositions.

	SiO_2	TiO_2	Al_2O_3	Cr_2O_3	MnO	MgO	CaO	Na_2O	K_2O	P_2O_5	Total
EH-EL	61.21	0.12	3.23	0.45	0.25	32.64	1.48	1.21	0.11	0.32	101.02
Mer10[a]	54.82	0.14	3.7	0.52	0.28	37.32	1.62	1.37	0.13	0.10	100.00
Mer20[a]	47.91	0.16	4.26	0.60	0.33	43.04	1.87	1.58	0.15	0.10	100.00
silicate-metal-sulfide used in the experiments											
	silicate	Fe	FeS	Bulk S content (%)							
0.2S	0.80	0.00	0.20	7.30							
0.1S	0.90	0.00	0.10	3.60							
0.05S	0.95	0.00	0.05	1.80							
0S	0.86	0.14	0.00	0.00							

[a] Considering a bulk silicate Mercury compositionally similar to the silicate fraction of an enstatite chondrite with 10% and 20% Si partitioned into Mercury's core (compositions Mer10 and Mer20). This assumes that Mercury's core is 70 wt.% of Mercury's bulk mass (Hauck et al., 2013) and contains 2.5 and 5 wt.% Si (Malavergne et al., 2010).

Table 2
Experimental conditions and run products.

sample	T (°C)	P (GPa)	Fe or S source	Time (min)	ΔIW(Si-SiO$_2$)[a]	Experimental phases	S$_{(Sil)}$[b]
Mer10							
A21	1650	3	0.2 FeS	30	−6.5	Gl (83), Ens (17), FeSi, FeS, FeMgS	6.26*
A22	1675	3	0.2 FeS	30	−6.5	Gl, FeSi, FeS, FeMgS	6*
A23	1700	3	0.2 FeS	20	−6.5	Gl, FeSi, FeS, FeMgS	6.79*
A11	1675	3	0.1 FeS	30	−7.4	Gl (92), Ens (8), FeSi	4.82
A12	1700	3	0.1 FeS	30	−7.3	Gl, FeSi	3.46
A13	1725	3	0.1 FeS	30	−7.3	Gl, FeSi	3.86
A051	1725	3	0.05 FeS	60	−7.4	Gl (99), Fo (<1), FeSi	1.44
A052	1750	3	0.05 FeS	46	−7.3	Gl, FeSi	1.35
A052	1775	3	0.05 FeS	30	−7.2	Gl, FeSi	1.46
A01	1750	3	0.14 Fe	30	−6.8	Gl (99), Fo (<1), FeSi	0
A02	1775	3	0.14 Fe	40	−6.8	Gl, FeSi	0
a21	1775	5	0.2 FeS	30	−6.7	Gl (79), Ens (21), FeSi, FeS	5.88*
a22	1800	5	0.2 FeS	20	−6.5	Gl, FeSi, FeS	5.31*
a23	1825	5	0.2 FeS	20	−6.6	Gl, FeSi, FeS	5.77*
a11	1800	5	0.1 FeS	60	−7.5	Gl (66), Ens (34), FeSi	4.41
a12	1825	5	0.1 FeS	30	−7.3	Gl, FeSi	2.95
a13	1850	5	0.1 FeS	20	−7.1	Gl, FeSi	3.7
a051	1825	5	0.05 FeS	60	−7.4	Gl (62), Ens (38), Fo**, FeSi	1.68
a052	1850	5	0.05 FeS	60	−7.4	Gl, FeSi	1.52
a053	1875	5	0.05 FeS	60	−7.2	Gl, FeSi	1.17
a01	1850	5	0.14 Fe	30	−6.9	Gl (67), Ens (33), Fo**, FeSi	0
a02	1875	5	0.14 Fe	50	−6.7	Gl, FeSi	0
a03	1900	5	0.14 Fe	40	−6.7	Gl, FeSi	0
Mer20							
B21	1650	3	0.2 FeS	30	−6.5	Gl (76), Fo (24), FeSi, FeS, FeMgS	6.36*
B22	1675	3	0.2 FeS	30	−6.2	Gl (79), Fo (21), FeSi, FeS, FeMgS	5.74*
B23	1700	3	0.2 FeS	20	−6.1	Gl, FeSi, FeS, FeMgS	5.9*
B11	1675	3	0.1 FeS	30	−7.1	Gl (81), Fo (19), FeSi,	5.63
B12	1700	3	0.1 FeS	30	−7.1	Gl (94), Fo (6), FeSi	5.17
B13	1725	3	0.1 FeS	30	−6.5	Gl, FeSi	5.5
B14	1750	3	0.1 FeS	30	−5.8	Gl, FeSi, FeS	4.89*
B051	1725	3	0.05 FeS	60	−7.6	Gl (74), Fo (26), FeSi	2.84
B052	1750	3	0.05 FeS	46	−7.5	Gl (84), Fo (16), FeSi	2.9
B052	1775	3	0.05 FeS	30	−7.4	Gl (90), Fo (10), FeSi	2.3
B054	1800	3	0.05 FeS	20	−7.3	Gl, FeSi	2.25
B055	1825	3	0.05 FeS	20	−7.1	Gl, FeSi	1.99
B01	1750	3	0.14 Fe	30	−6.9	Gl (63), Fo (37), FeSi	0
B02	1775	3	0.14 Fe	40	−6.7	Gl (73), Fo (27), FeSi	0
B03	1800	3	0.14 Fe	30	−6.8	Gl (77), Fo (23), FeSi	0
B04	1825	3	0.14 Fe	30	−7.1	Gl (85), Fo (15), FeSi	0
B05	1850	3	0.14 Fe	30	−6.6	Gl (98), Fo (2), FeSi	0
B06	1875	3	0.14 Fe	20	−6.3	Gl (99), Fo (<1), FeSi	0
B07	1900	3	0.14 Fe	20	−6.1	Gl, FeSi	0
b21	1775	5	0.2 FeS	30	−6.7	Gl (86), Fo (14), FeSi, FeS	5.75*
b22	1800	5	0.2 FeS	20	−6.2	Gl (88), Fo (12), FeSi, FeS	5.16*
b23	1825	5	0.2 FeS	20	−5.9	Gl, FeSi, FeS	5.21*
b24	1850	5	0.2 FeS	20	−6.2	Gl, FeSi, FeS	5.95*
b11	1800	5	0.1 FeS	60	−7.0	Gl (82), Fo (18), FeSi	5.22
b12	1825	5	0.1 FeS	30	−6.7	Gl (88), Fo (12), FeSi, FeS	4.99*
b13	1850	5	0.1 FeS	20	−6.1	Gl (93), Fo (7), FeSi, FeS	4.19*
b14	1870	5	0.1 FeS	20	−6.3	Gl, FeSi, FeS	4.57*
b051	1825	5	0.05 FeS	60	−7.5	Gl (75), Fo (25), FeSi	2.58
b052	1850	5	0.05 FeS	60	−7.3	Gl (87), Fo (13), FeSi	2.53
b053	1875	5	0.05 FeS	60	−7.2	Gl (99), Fo (<1), FeSi	1.88
b054	1900	5	0.05 FeS	20	−7.3	Gl, FeSi	2.19
b055	1925	5	0.05 FeS	20	−7.1	Gl, FeSi	1.87
b01	1850	5	0.14 Fe	30	−7.1	Gl (68), Fo (32), FeSi	0
b02	1875	5	0.14 Fe	50	−6.9	Gl (81), Fo (19), FeSi	0
b03	1900	5	0.14 Fe	40	−6.7	Gl (85), Fo (15), FeSi	0
b04	1950	5	0.14 Fe	20	−6.4	Gl (94), Fo (6), FeSi	0
b05	1975	5	0.14 Fe	20	−6.2	Gl, FeSi	0
b06	2000	5	0.14 Fe	20	−6.4	Gl, FeSi	0

Abbreviations: Gl = silicate glass; Ens = enstatite; Fo = forsterite; FeS = sulfide melt dominated by Fe and S; FeMgS = sulfide melt dominated by Fe, Mg, and S; FeSi = metallic melt dominated by Fe and Si.

aOxygen fugacity relative to iron-wüstite calculated from Si-SiO2 equilibrium according to Cartier et al. (2014).

bSulfur content in silicate melt.

*Sulfide saturated experiments. ** Failed to be calculated by mass balance.

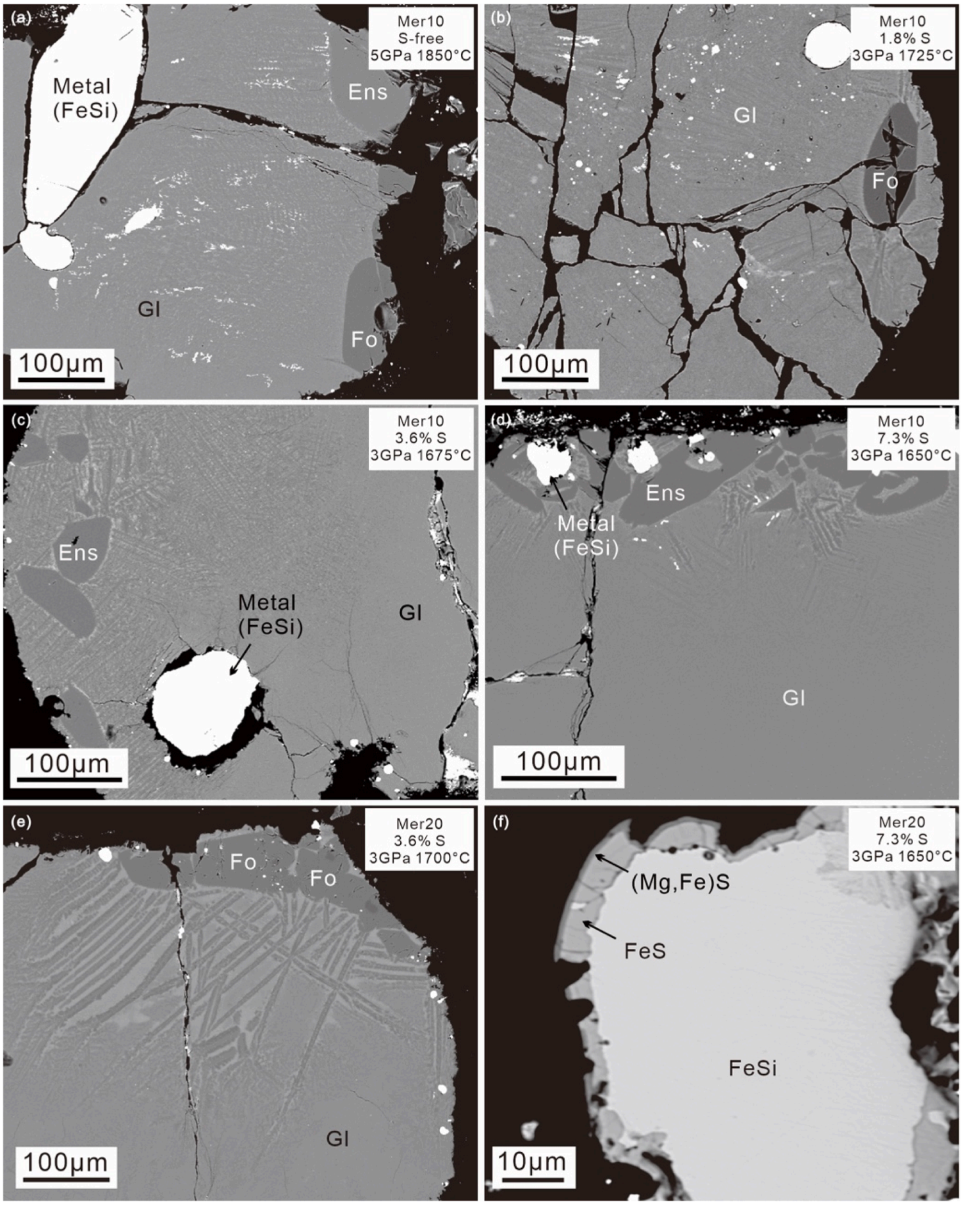

Fig. 1. Back-scattered electron images of representative experimental products. The starting compositions and experimental pressure-temperature conditions are listed on the top-right of each panel. Abbreviations: Gl = silicate glass; Ens = enstatite; Fo = forsterite.

equilibrium between metallic alloy and silicate melt (Cartier et al., 2014; Namur et al., 2016b):

$$Si^{Met} + O_2 = SiO_2{}^{Sil} \tag{1}$$

The thermodynamic relationship is expressed as:

$$fO_2 = \exp\left(\frac{-\Delta G^0}{RT}\right)\cdot\frac{a_{SiO_2}}{a_{Si}} \tag{2}$$

where a_{SiO_2} ($X_{SiO_2} \cdot \gamma_{SiO_2}$) is the activity of SiO_2 (X is the mole fraction and γ is the activity coefficient) in the silicate melt (a_{SiO_2} Mer10 = 0.55; a_{SiO_2} Mer20 = 0.35 as calculated at their S-free liquidus temperature with MAGEMin; Green et al., 2025; Riel et al., 2022). Meanwhile, the exact value of a_{SiO_2} has little influence on fO_2, as demonstrated by Saracino et al. (2025) and show in Supplementary Fig. S2. a_{Si} ($X_{Si} \cdot \gamma_{Si}$) is the activity of Si in the metallic phase and computed using the Oxford metal activity calculator. $\Delta G^0$is the free energy for reaction (1) at 1 bar, which calculated using the data from Robie and Hemmingway. (1995). fO_2 is reported relative to the iron-wustite (IW) buffer as:

$$\Delta IW = \log fO_{2;Ex} - \log fO_{2;IW} \tag{3}$$

Where $\log fO_{2;IW}$ calculated from Huebner (1971):

$$\log fO_{2;IW} = 6.57 - \frac{27215}{T(K)} + 0.055\frac{P(bar) - 1}{T(K)} \tag{4}$$

Experimental fO_2 values range from IW-5.8 to IW-7.6 (Table 2) with estimated error ±0.5 log units.

3. Results

3.1. Attainment of equilibrium

The attainment of equilibrium in crystallization experiments requires that the run duration is long enough to grow compositionally homogeneous minerals in thermodynamic equilibrium with the silicate melt, but that the run duration is short enough to avoid alkali and volatile loss. To evaluate whether this duration was sufficient, we performed time-series (5–60 min) experiments on a representative composition (Mer20 + 0.10FeS) at 3 GPa and 1700 °C (Fig. 2). In the 5 min experiment, no mineral was found whereas olivine is observed in longer experiments. Between 15 and 30 min, both silicate melt sulfur contents and mineral compositions remained constant. At 60 min, the melt sulfur content showed only a slight decrease (Fig. 2a), while Na_2O loss became more pronounced (Fig. 2b). These results demonstrate that 20–30 min is sufficient to achieve equilibrium while minimizing volatile loss under our experimental conditions. At the high Mercury-relevant temperatures studied here (1650–2000 °C), rapid diffusion kinetics (Zhang et al., 2010) further support that equilibrium was closely approached in our experiments. See detail data in Supplementary Data 1.

3.2. Phase assemblages and chemical composition

All super-liquidus experiments produced a two-phase assemblage of silicate glass and metallic alloy. Runs with 7.3 wt.% S in Mer10 and Mer20, and those with 3.6 wt.% S in Mer20, additionally contained a sulfide melt phase encasing the metallic alloy (Fig. 1f; Table 2). This reflects liquid immiscibility in the Fe-Si-S system at moderately low pressure (Morard and Katsura, 2010). Sub-liquidus experiments yielded additional crystalline phases, whose identities vary with composition and P-T conditions. In all Mer20 experiments, forsterite is the liquidus phase (Figs. 1e; 3 and 4). In Mer10, enstatite dominates the liquidus phase in runs containing 3.6–7.3 wt.% S at 3–5 GPa (Fig. 1c-d; 3 and 4). At lower sulfur contents (1.8 wt.% S) and in S-free systems, forsterite crystallizes at 3 GPa (Fig. 1b; 3 and 4), while both forsterite and enstatite coexist on the liquidus at 5 GPa (Fig. 1a; 3 and 4).

Major element compositions of the silicate melt in super-liquidus run products are very similar to the starting compositions with some S incorporated in S-bearing experiments (Supplementary Dataset 1). For the sub-liquidus experiments, the major element compositions of residual silicate melts are affected by the crystallization of enstatite and forsterite. The crystallization of enstatite mostly affects the composition of silicate melt by decreasing the content of MgO and SiO_2, while forsterite crystallization changes the composition of silicate melt by decreasing MgO content and increasing SiO_2 content. Enstatite is a pure Mg-endmember enstatite with minor Al_2O_3 (0.33–1.22 wt.%). We note a slight increase in Al_2O_3 with increasing pressure. Forsterite is a pure forsterite endmember.

The sulfur contents in silicate melts are reported in Table 2. In sulfide-saturated conditions at 3 GPa, the sulfur contents for Mer10 and Mer20 range respectively from 6.00–6.79 wt.% and 4.89–6.36 wt.%. These values are lower at 5 GPa, with ranges of 5.31–5.88 wt.% for Mer10 and 4.19–5.95 wt.% for Mer20. In sulfide undersaturated conditions, we observe lower S contents at 3 GPa (Mer10: 0–4.82 wt.%; Mer20: 0–5.63 wt.%) and 5 GPa (Mer10: 0–4.41 wt.%; Mer20: 0–5.22 wt.%). The sub-liquidus sulfide undersaturated experiments have a higher sulfur concentration than that of super-liquidus and near-liquidus experiments due to the crystallization of minerals which decreases the proportion of silicate melt. Sulfur behaves as highly incompatible element and is virtually absent in these minerals (Supplementary Dataset1), thereby increasing the S content in the residual melt.

Metal alloys are dominated by Fe (68.42–90.85 wt.%) and Si (4.42–21.81 wt.%), with minor Cr (0.06–5.35 wt.%), P (0.03–4.34 wt.%), and S (0–1.42 wt.%). In sulfide undersaturated experiments, metal alloys also contain Mn and Ti. We observe a negative correlation between the amount of FeS in the starting composition and the alloy Si content, which is explained by the slightly more oxidizing conditions in experiments with addition of more FeS (Namur et al., 2016a). In sulfide-saturated experiments, the sulfide phase is made up of Fe (31.59–56.95 wt.%) and S (35.05–37.03 wt.%), with minor Ti (0.13–2.37 wt.%), Cr (3.63–23.63 wt.%), Mn (0.44–2.25 wt.%), and Mg (0.01–0.26 wt.%). In experiments on 0.2FeS Mer10 and Mer20 compositions at 3 GPa, we observe a second sulfide melt (Fig. 1f). Although, the region is too small to be accurately measured by EMPA, it is supposed to be FeMgS, according to previous studies (Namur et al., 2016a; Saracino et al., 2025; Xu et al., 2024).

3.3. Liquidus temperatures

Using the calculated melt proportions (Fig. 3) and the observed phase relationships obtained from BSE images (Fig. 1), we bracketed the liquidus of Mer10 and Mer20 at 3 and 5 GPa with variable S contents. For sulfur-free compositions, at 3 GPa, the first super-liquidus experiment of Mer10 is reached at 1775 °C, where forsterite melts out. At 5 GPa, the first S-free super-liquidus experiment is at 1875 °C, with forsterite and enstatite disappearing simultaneously. Given the 25 °C step between successive experiments, we therefore estimated the liquidus temperature to 1762.5 ± 12.5 °C at 3 GPa, and to 1862.5 ± 12.5 °C at 5 GPa. Similarly, we constrain the S-free liquidus of Mer20 at 1887.5 ± 12.5 °C at 3 GPa and 1962.5 ± 12.5 °C at 5 GPa.

The addition of sulfur lowers the liquidus significantly: with 1.8 wt.% S added to the bulk composition, the liquidus temperatures of Mer10 decrease to 1737.5 ± 12.5 °C (3 GPa; with 1.35 wt.% S in silicate melt) and 1837.5 ± 12.5 °C (5 GPa; with 1.52 wt.% S in silicate melt), and for Mer20 to 1787.5 ± 12.5 °C (3 GPa; 2.25 wt.% S) and 1887.5 ± 12.5 °C (5 GPa; 2.19 wt.% S). With 3.6 wt.% S added, the liquidus of Mer10 is further depressed to 1687.5 ± 12.5 °C (3 GPa; 3.46 wt.% S) and 1812.5

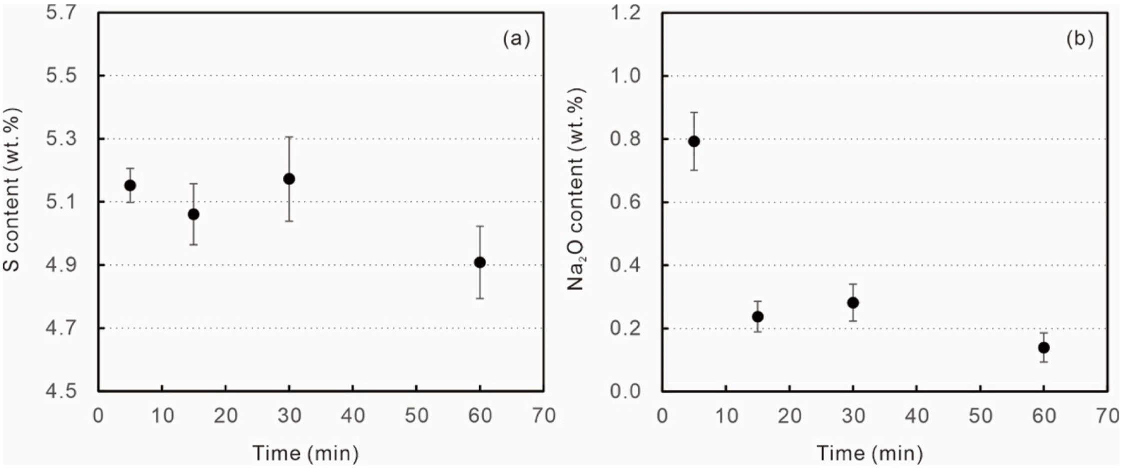

Fig. 2. S and Na_2O contents of silicate melts as a function of experimental duration. The experiments conducted at 3 GPa and 1700 °C, and the fO_2 ranges from IW-7.1 to IW-6.3.

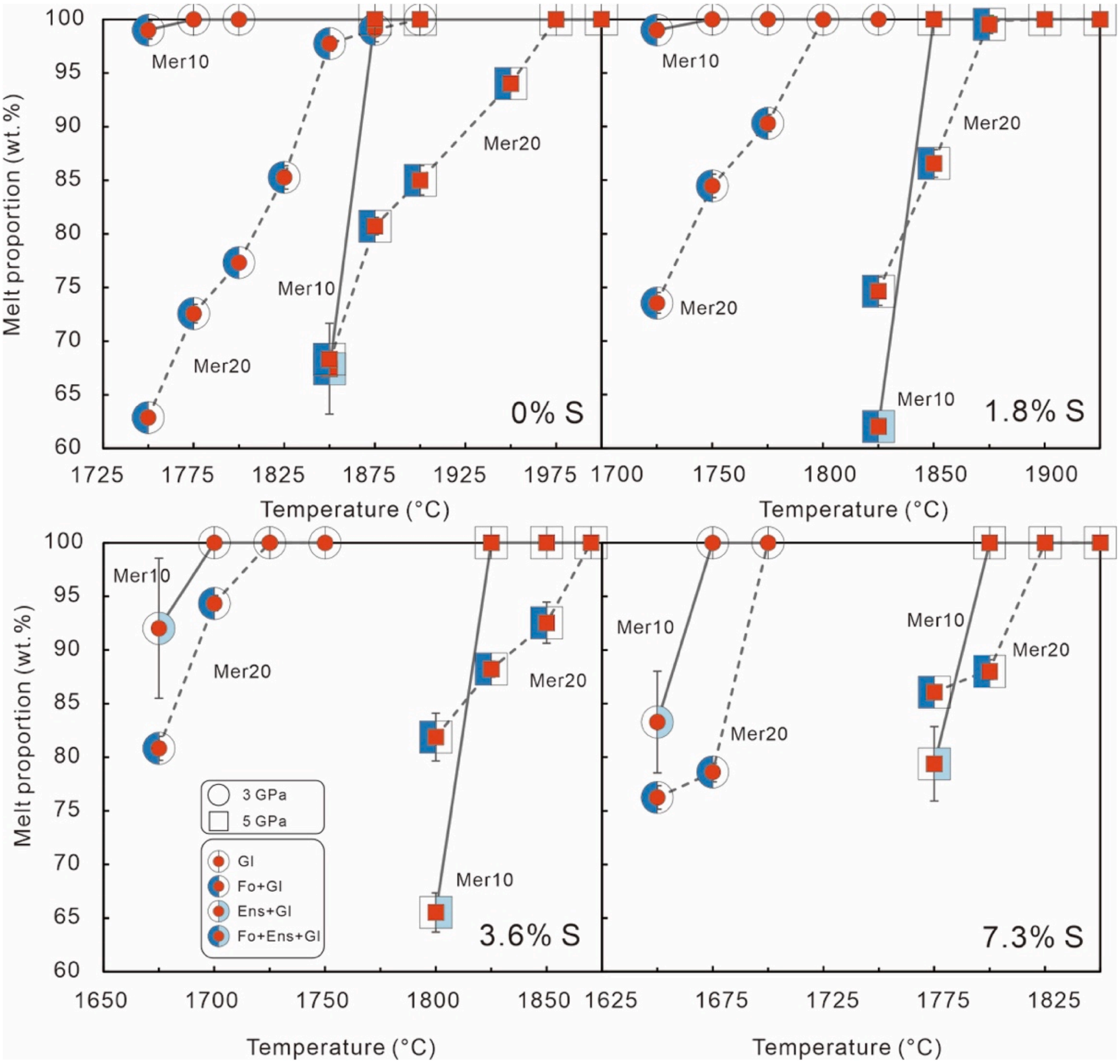

Fig. 3. Melt proportion and phase relations for compositions Mer10 and Mer20 as a function of temperature at 3 GPa and 5 GPa. Solid lines denote the Mer10 composition, while dashed lines the Mer20 composition. The corresponding S content for each set of experiments is shown in the bottom right corner of each panel. Melt proportions are calculated based on mass balance using EPMA data.

± 12.5 °C (5 GPa; 2.95 wt.% S), as is the liquidus of Mer20 is 1712.5 ± 12.5 °C (3 GPa; 5.5 wt.% S) and 1860 ± 12.5 °C (5 GPa; 4.57 wt.% S). For compositions with 7.3 wt.% S added, the lowest liquidus values are observed: 1662.5 ± 12.5 °C (Mer10; 3 GPa; 6 wt.% S), 1787.5 ± 12.5 °C (Mer10; 5 GPa; 5.31 wt.% S), and 1687.5 ± 12.5 °C (Mer20; 3 GPa; 5.9 wt.% S), 1812.5 ± 12.5 °C (Mer20; 5 GPa; 5.21 wt.% S). Our results therefore show a clear negative correlation between liquidus temperature and sulfur content in silicate melt (Fig. 5).

4. Discussion

4.1. Sulfur-driven liquidus depression

Sulfur dissolving into silicate melt under highly reduced conditions is known to form MgS and CaS complexes (Anzures et al., 2020, 2025; Boujibar et al., 2025; Namur et al., 2016b). In the Fo-En-Qz phase diagram (Fig. S3; Andersen, 1915; Liu and Presnall, 1990; Longhi, 1987), these S-induced complexes modify melt structure and shift phase equilibria (Fig. 4). For Mer10, sulfur-driven MgS complexation at IW-7.5 to IW-6.5 increases the effective activity of SiO_2 in the melt (Anzures et al., 2020, 2025), pushing the melt composition toward the enstatite stability field and promoting enstatite saturation (Boujibar et al., 2025). In contrast, the higher MgO content of Mer20 maintains forsterite as the liquidus phase despite sulfur addition or pressure increase. Pressure additionally shifts the Fo-En boundary to higher silica activity, expanding the enstatite stability field (Andersen, 1915; Liu and Presnall, 1990; Sen and Presnall, 1984) and producing the observed coexistence of forsterite and enstatite in high-pressure Mer10 experiments.

At fixed pressure, the liquidus temperature of a magma is strongly composition-dependent. Mercurian magmas are particularly sensitive to sulfur because S interacts with network-modifying cations (mainly Mg^{2+}) and can substitute for O^{2-} in the melt structure (Anzures et al., 2020, 2025; Fogel, 2005; Métrich et al., 2009; Zolotov et al., 2013). These structural modifications alter the activities of major oxides (Pommier et al., 2023), thereby lowering the saturation state of the melt with respect to primary silicate phases (olivine and orthopyroxene) at constant temperature. As a result, sulfur reduces the liquidus and enhances melt stability across the Mercurian mantle compositions investigated.

The effect of sulfur on the Mercurian mantle liquidus is here quantified by the temperature difference (ΔT) between sulfur-free (T_{S-free}) and sulfur-bearing (T_S) compositions, where $\Delta T = T_{S-free} - T_S$ (°C). As shown in Fig. 6a, the liquidus depression of silicate melt is positively correlated with sulfur concentrations, negatively correlated with pressure, and compositionally-sensitive with a larger S-effect on a higher Mg/Si melt (i.e. olivine liquidus).

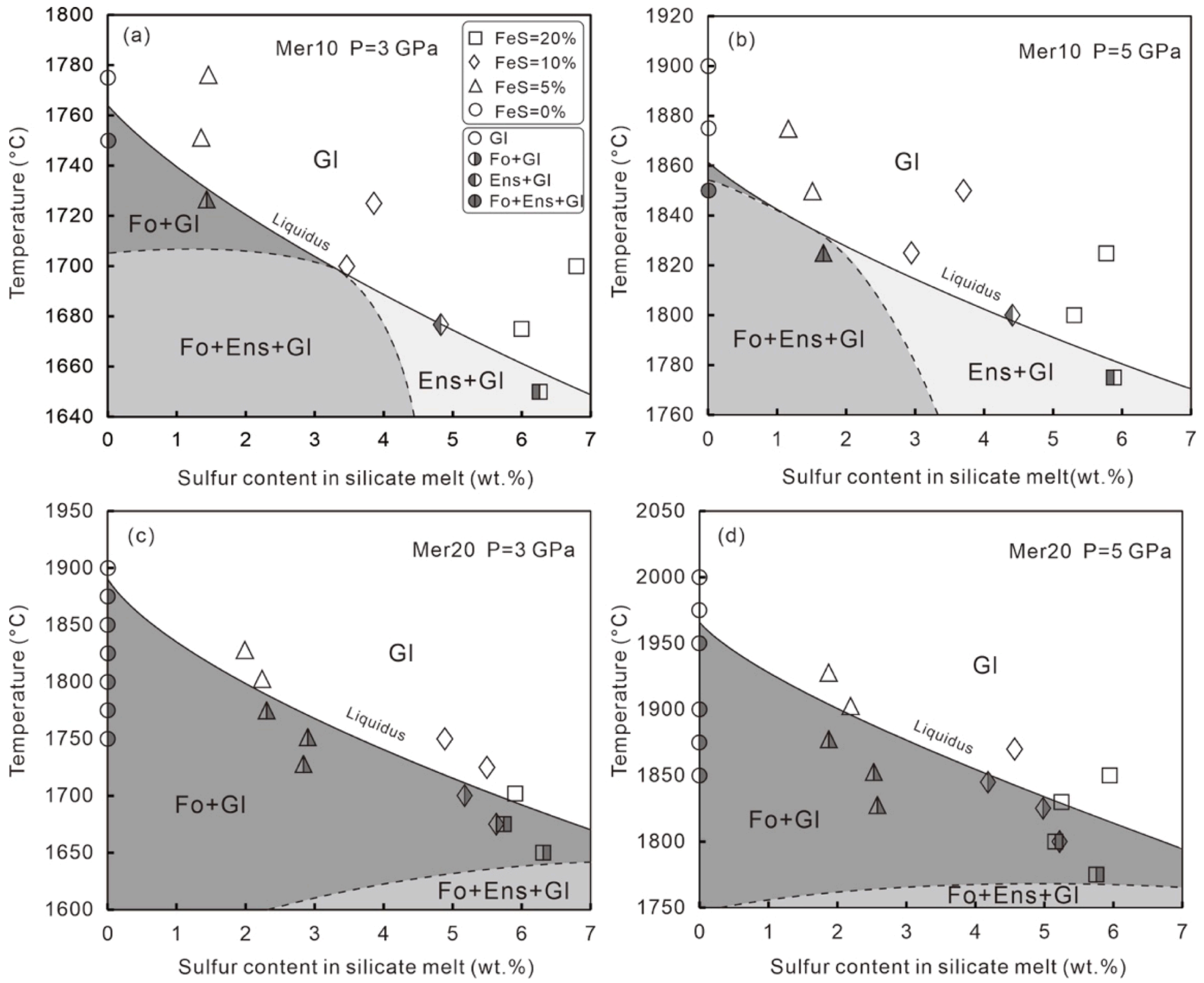

Fig. 4. Experimental phase diagrams of Mer10 and Mer20 compositions. Note that y-axis scales differ between panels. The liquidus curves are identical to those presented in Fig. 5. (a) At 3 GPa, the liquidus for Mer10 is systematically depressed with increasing S content, and the stable liquidus phase changes from forsterite to enstatite. (b) At 5 GPa, the liquidus of Mer10 follows a similar depression trend, and the liquidus phase shifts from forsterite + enstatite to enstatite alone. (c), (d) The liquidus depression for Mer20 at 3 GPa and 5 GPa shows similar trend, and forsterite remains the sole liquidus phase throughout the sulfur range investigated.

Following the approach to model the effect of water on the solidus of the Earth mantle (Hirschmann et al., 2009), we use a simple cryoscopic approach. In this thermodynamic framework, the depression of the liquidus temperature is quantitatively related to the mole fraction of the dissolved volatile and the molar entropy of fusion of the silicate melt. Benchmarked against our experiments, this approach allows us to quantify the relationship between the mole fraction of dissolved sulfur in silicate melt (X_S) and the liquidus temperature (T_S) relative to the sulfur-free liquidus (T_{S-free}; Fig. 6b) as expressed by:

$$T_S = \frac{T_{S-free}}{(1 - (R/(M \cdot \Delta S)) \cdot \ln (1 - X_S))} \tag{5}$$

Where ΔS is the entropy of fusion per unit mass for Mercurian melts; M is the number of grams in one mole of silicate for which we adopt a value of a mean molar weight for Mer10 (51.6 g/mol) and Mer20 (50.5 g/mol); R is the gas constant. We note that for all compositions (Mer10 and Mer20) and pressure conditions, experiments at different S contents can be fitted using a constant ΔS value for each specific condition: 0.3 $J/\mathrm{K}\cdot\mathrm{g}$ (Mer10 at 3 GPa), 0.4 $J/\mathrm{K}\cdot\mathrm{g}$ (Mer10 at 5 GPa), 0.14 $J/\mathrm{K}\cdot\mathrm{g}$ (Mer20 at 3 GPa) and 0.12 $J/\mathrm{K}\cdot\mathrm{g}$ (Mer 20 at 5 GPa). The two values of Mer20 are slightly lower than those of water-bearing melts (0.25–0.4 $J/\mathrm{K}\cdot\mathrm{g}$) (Kojitani and Akaogi, 1997; McKenzie and Bickle, 1988), and the minor increase in ΔS with pressure agrees with literature (Kojitani and Akaogi, 1997). Although dissolved sulfur likely raises the configurational entropy of the melt, its contribution to the entropy difference between solid and liquid appears nearly constant across our S range, allowing all experiments to be reproduced with a single ΔS.

The adequate fitting of our experimental data with a cryoscopic model attests the thermodynamic validity of the liquidus depression that we observe (Fig. 6b). As such, we combined our experimental data with literature results (Saracino et al., 2025) and parameterized equations that link the liquidus depression to the melt S content and the pressure conditions using a power law model (Eqs. (6)-(7)), which is similar to that used by Almeev et al. (2007) for water-induced liquidus depression and by Filiberto et al. (2012) for F and Cl (see details in Fig. S4):

$$\Delta T_{Mer10} = (33.5 - 3.10 \cdot P) \cdot C_S^{0.81} \; (\mathrm{R}^2 = 0.90) \tag{6}$$

$$T_{Mer20} = (75.6 - 6.16 \cdot P) \cdot C_S^{0.67} \; (\mathrm{R}^2 = 0.97) \tag{7}$$

where C_S is the sulfur concentration in melt (wt.%); P is the pressure in

GPa. The comparison between the two equations and the experimental data is presented in Fig. S4. The relatively large decrease of the liquidus for Mer20 compared to Mer10 at constant S contents can be attributed to the contrasting a_{SiO_2} in their bulk compositions. As observed in simplified Fo-An-Qz systems (Fig. S3), increasing the silica activity has a stronger influence on the relative position of forsterite and enstatite phase boundary for Mer20 than Mer10 and therefore on the pressure shift due to the formation of MgS, which leads to more significant liquidus temperature depression.

Our results indicate that sulfur play the same role as other volatiles (e.g., water, oxygen and chlorine) to depress the liquidus temperature (Filiberto and Treiman, 2009; Lin et al., 2021; Lin and van Westrenen, 2021; Sisson and Grove, 1993). Compared with other volatiles (H_2O, F, Cl; Almeev et al., 2012, 2007; Filiberto et al., 2012; Médard and Grove, 2008), sulfur exerts an equally significant effect on the liquidus (Fig. 6a). However, the phenomenon arises through distinct mechanisms: H_2O primarily depolymerizes melts by breaking bridging oxygen bonds in the silicate network (Zeng et al., 1999), whereas S, Cl and F form complexes in the melt that affect cation activity and viscosity (Mouser et al., 2021), thereby shift the liquidus down, increase orthopyroxene stability (Fig. 4; Anzures et al., 2025, 2020; Filiberto et al., 2012; Filiberto and Treiman, 2009; Pommier et al., 2023). Furthermore, similarly to H_2O (Almeev et al., 2007; Koch et al., 2025), sulfur exhibits a more pronounced effect on the liquidus of olivine than orthopyroxene at equivalent pressures. This large effect, supported by our thermodynamic analysis, necessitates explicit incorporation of sulfur speciation and concentration in models of mantle evolution, particularly regarding the mantle thermal state and magma ocean crystallization (Namur et al., 2016b).

4.2. Implications for the partial melting of Mercury-like mantle

Our experimental results also provide constraints on the sulfur content of Mercury's magma ocean at sulfide saturation, and therefore on the sulfur budget of the mantle prior to formation of the secondary volcanic crust. As shown by our S-saturated experiments (fO_2 = IW-6.7 to IW-5.8; Table 2), bulk silicate Mercury compositions are expected to contain ~5–7 wt.% S. These values are in the lower range as compared to those previously inferred 7–11 wt.% S (Namur et al., 2016a).

Recognizing sulfur as a major mantle component, we evaluated the degree of melting (*F*, defined as the equilibrium weight fraction of melt) during mantle melting for the Mer10 and Mer20 mantle compositions. We adopt a parameterization analogous to that developed by Katz et al. (2003) for H_2O-bearing melting of Earth's mantle, modified here to account for sulfur-induced solidus depression:

$$F(T,P) = \left(\frac{T - T_{solidus}(P)}{T_{liquidus}(P) - T_{solidus}(P)}\right)^{1.5} \tag{8}$$

Here, $T(P)$ represents the temperature at a given pressure. The exponent of 1.5 is adapted from Katz et al. (2003), and the influence of this value is evaluated in Fig. S5. The liquidus temperatures ($T_{liquidus}$) were directly constrained by our experimental data (Figs. 3–5). In our model, the temperature interval between solidus and liquidus remains unchanged as a function of the mantle S content. However, sulfur shifts solidus and liquidus curves to lower temperature compared to S-free systems which is expected to increase the melt fraction at any given temperature (T). Eq. (8) can be further expressed as:

$$F(T,P) = \left(\frac{T - \left(T^{S-free}_{solidus}(P) - \Delta T\right)}{T^{S-free}_{liquidus}(P) - T^{S-free}_{solidus}(P)}\right)^{1.5} \tag{9}$$

where $T^{S-free}_{liquidus}$ is the sulfur-free liquidus. Similar to the assumption of Katz et al. (2003) for H_2O, we consider that the effect of S on the solidus depression is similar to that on the liquidus depression. In the numerator of Eq. (9), we therefore use ΔT as being the sulfur-induced liquidus depression (from Eqs. (6)–(7)). For the solidus of sulfur-free compositions, we use the expression obtained by Namur et al. (2016b):

$$T^{S-free}_{solidus} = 1148 + 177P - 12.2P^2 \tag{10}$$

where *P* is in GPa.

Based on experimental results and thermodynamic modelling, Namur et al. (2016b) derived melting degrees and corresponding mantle potential temperature (T_P) values required to produce different geochemical provinces on Mercury. However, our new calculations reveal that sulfur may profoundly enhance partial melting of primitive Mercury-like compositions at depth (Fig. 7), which means that a similar amount of melt could have been produced at significantly lower T_P than previously estimated. For the High-Mg province, where lavas exhibit the highest sulfur concentrations (typically 2.5–3 wt.% S; Namur et al., 2016a), mantle sources with comparable or higher sulfur contents could enhance partial melting by 20–40% at 5 GPa (Fig. 7b and d). To achieve the ~50% melt fraction of this province, the required T_P calculated by Namur et al. (2016b) was 1650 °C. Here, we re-evaluate this in light of our new melting parameterization (Fig. 7). Comparing our experiments and their parameterization at a given temperature between 3 and 5 GPa, we find that adiabatic melting could produce as much as 20% of melt per GPa of decompression. This value is higher than the values calculated by Namur et al. (2016b) (12.5 %/GPa). This means that decompression over 2–3 GPa might sufficient to produce the

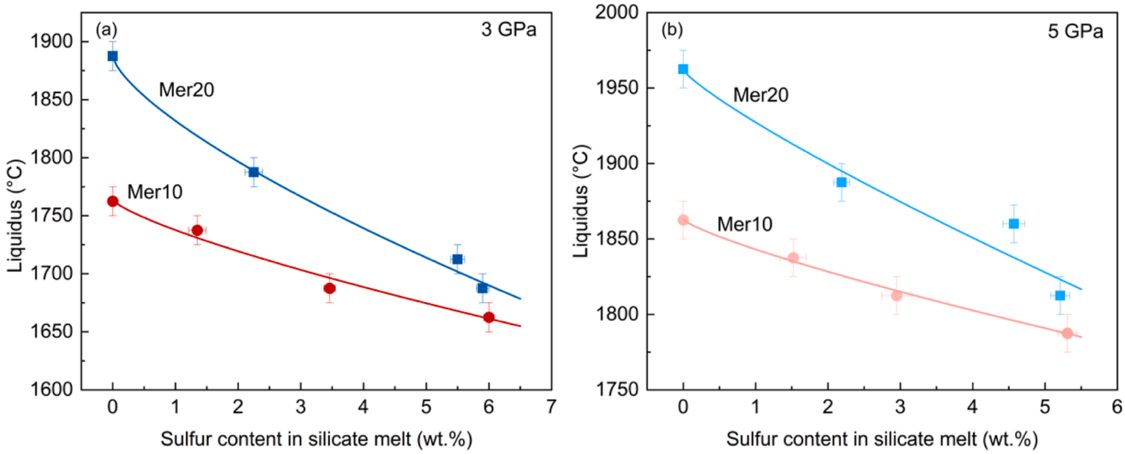

Fig. 5. The liquidi of Mer10 and Mer20 as a function of sulfur contents in the silicate melts. The error bars for Y axis and X axis are 25 °C and the one standard deviation of S content in silicate melt respectively (see detail in Supplementary Dataset 1).

high-degree melting necessary to produce the High-Mg province. Accordingly, assuming an adiabatic profile of 10 K/GPa as calculated with MAGEMin, we estimate that a mantle T_P of 1600 °C is sufficient to produce the High-Mg province.

The Intercrater Plains (IcP), Northern Volcanic Plains (NVP) and Smooth Plains (SP) displayed relatively lower sulfur contents (1.6–2 wt. %; Namur et al., 2016a; Weider et al., 2015). Thermodynamic simulations indicate that these lavas originate from shallower depth in mantle (Namur et al., 2016a). For these regions, our models predict a 20–30% enhancement in partial melting at 3 GPa (Fig. 7a, c). For those, we calculate a mantle T_P of 1375–1470 °C, slightly lower than those calculated by Namur et al. (2016b) (1400–1525 °C). Collectively, these revisions of melting temperatures highlight sulfur's critical role in lowering melting conditions on Mercury, enabling to extend or trigger magmatism at lower mantle potential temperatures (Prockter et al., 2010), which demonstrates the highly fertile of Mercurian mantle.

4.3. *The role of sulfur on the lithological variability of the mantle*

The liquidus depression caused by sulfur (Figs. 4 and 6; Eqs. (6)–(7)) may have profound implications for the thermal evolution and crystallization behavior of Mercury's primordial magma ocean (MO). To assess these effects, we adopted an analytical approach to model the cooling timescale and solidification dynamics.

We calculated the surface temperature of Mercury 4.5 Gyr ago (equilibrium temperature, T_{eq}) based on the Stefan-Boltzmann law:

$$T_{eq} = \left(\frac{(1 - A_B)S_{Mercury}f_{\Theta}}{4\sigma}\right)^{(1/4)} \tag{11}$$

where A_B is the albedo, $S_{Mercury}$ is the solar flux, and f_{Θ} is the attenuation of Sun's luminosity at 4.5 Gyr, and σ is the Stefan-Boltzmann Constant, and the resulting T_{eq} is approximately 388 K. This equation defines the temperature difference ($\Delta T_C = T_P - T_{eq}$) across the crust or boundary layer, which drives the diffusive cooling of the magma ocean. As discussion above, the cooling of the magma ocean is governed by its liquidus, and then the sulfur-induced liquidus depression inherently lowers the T_P (potential temperature). This consequently reduces the driving temperature difference ΔT_C, thereby decreasing the heat flux across the (graphite) crust (Fig. 8a). Given that the total amount of heat to be dissipated remains largely unchanged, this reduced rate of heat loss fundamentally extends the total time required for complete solidification.

Therefore, the cooling timescale of the magma ocean (τ_C, years; Fig. 8b) was estimated using the heat balance formulation adapted from Mouser et al. (2021):

$$\tau_C = \frac{L_H 0.2M_m + C_{p,\ mo}\Delta T_m 0.2M_m}{\left(\frac{\Delta T_C \kappa C_{p,\ g}\rho_g}{z}\right)A_{mo}} \tag{12}$$

where $0.2M_m$ scales the MO mass to represent the stage where 20% liquid remains (after 80% crystallization), L_H is the latent heat, $C_{p,\ mo}$ is the specific heat of the MO, ΔT_m is the temperature drop of the magma ocean during solidification, κ is the thermal diffusivity of graphite, $C_{p,\ g}$ is the thermal heat capacity of graphite, ρ_g is the density of graphite, z is the thickness of the graphite crust, and A_{mo} is the surface of magma ocean. All values used in this calculation are given in Mouser et al. (2021).

We use the solidus as Eq. (10) and calculated S-free liquidus temperature using the MAGEMin algorithm (Riel et al., 2022) and the thermodynamic database of Holland et al. (2018) based on the Mercury's mantle composition:

$$T_{sol} = 1148 + 177P - 12.2P^2 \tag{13}$$

And

$$T_{liq} = 1710 + 47.6P + 1.91P^2 \tag{14}$$

where P is in GPa. Consequently, we can calculate the cooling time scale for S-free scenario (τ_0). By incorporating our experimentally determined sulfur-induced liquidus depression, we can obtain the extended cooling duration $\Delta\tau$ ($\tau_C - \tau_0$; Fig. 8b).

While sulfur is known to depress the liquidus and solidus temperatures (Eqs. (6)–(7)), our sensitivity analysis indicates that its effect on the absolute cooling timescale is strongly coupled with the thickness of the overlying graphite crust. However, the relative cooling time extension is entirely independent of the crust thickness. For a thin graphite crust (< 10 m), the high efficiency of conductive cooling means that the liquidus depression of up to 200 °C results in a seemingly negligible extension of the cooling time (< 1 year; Fig. 8b). Nevertheless, because the baseline cooling time in a S-free scenario is also extremely short, the relative impact of sulfur remains significant. As the graphite crust thickness increases (> 100 m to 10,000 m), the insulating effect becomes significant (Fig. 8b). In this regime, the lower crystallization temperatures induced by sulfur can extend cooling duration by hundreds to

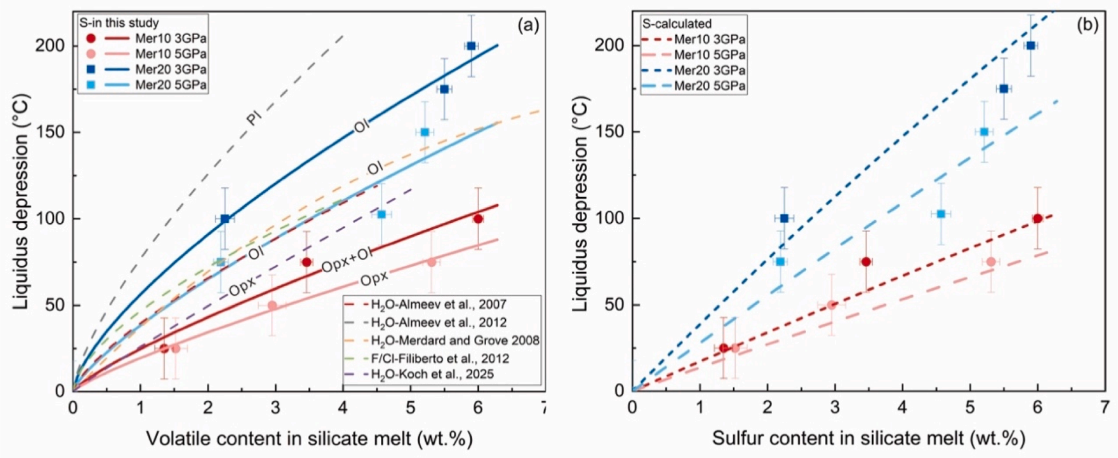

Fig. 6. Liquidus depression as a function of the volatile content in silicate melts, constrained by (a) Empirical regressions of ΔT based on our experimental data; the solid lines represent S in this study (see detailed regression formulas in Fig. S4), and the dashed lines show the role of H_2O, F and Cl from the literature (Almeev et al., 2007, 2012; Filiberto and Treiman, 2009; Filiberto et al., 2012; Koch et al., 2025; Médard and Grove, 2008), and (b) Calculations of the liquidus depression using a cryoscopic approach (Hirschmann et al., 2009); the dashed lines represent the calculation results using the thermodynamic model of Eq. (5). The mineral label in each line represents the liquidus phase.

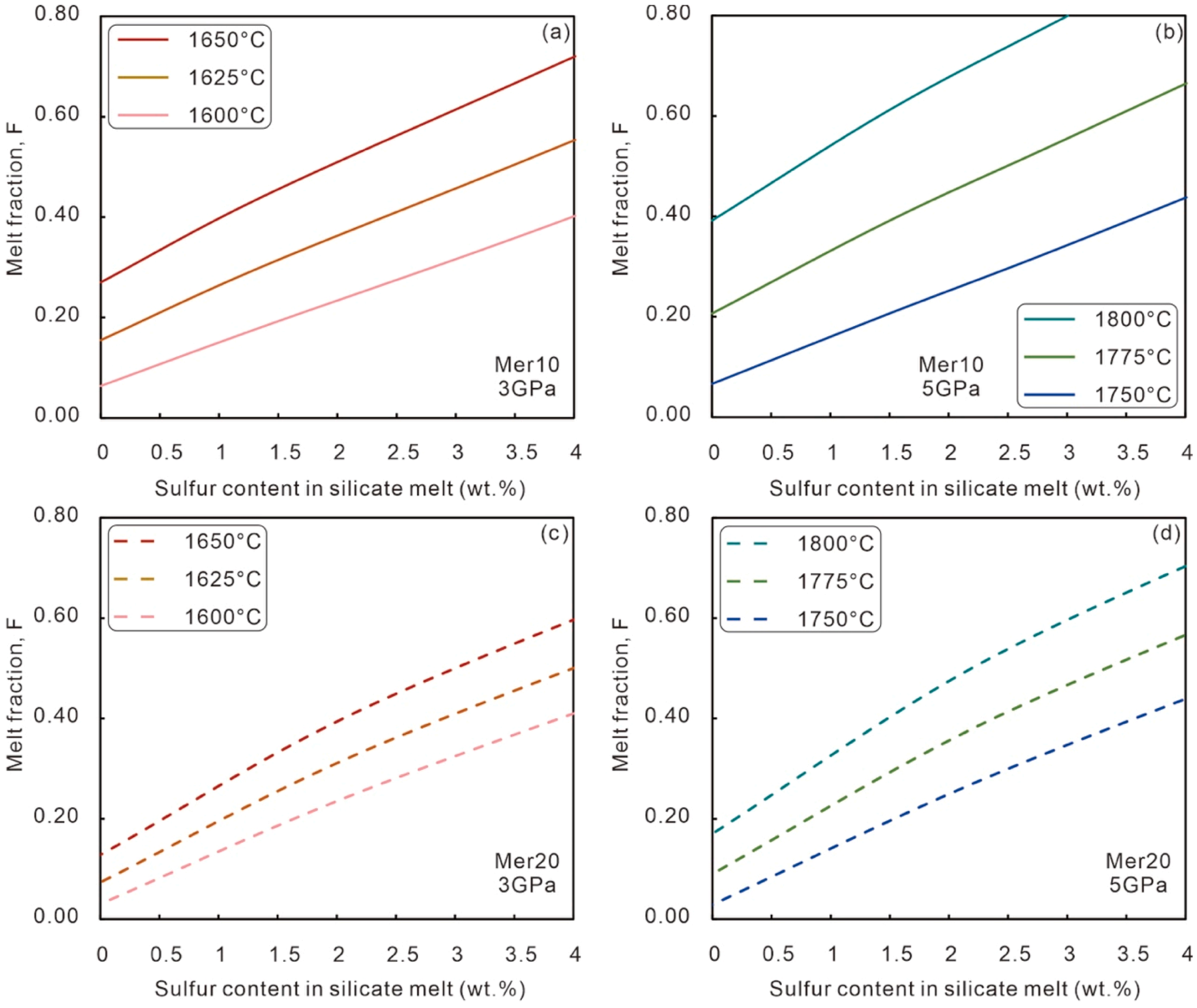

Fig. 7. Melt fraction as a function of the sulfur contents in the silicate melt at the pressures of 3 and 5 GPa and 1600–1800 °C. The selected temperatures for 3 GPa and 5 GPa are set to match the modeled temperatures at which melting begins at the two pressures on Mercury, following Namur et al. (2016b).

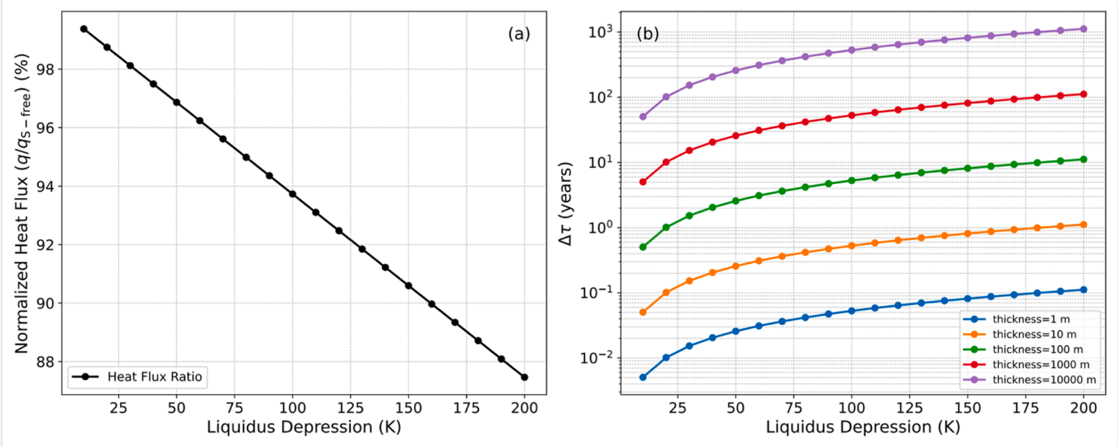

Fig. 8. Influence of sulfur-induce liquidus depression and graphite thickness on magma ocean cooling timescales. (a) The normalized heat flux ($q/q_{S\text{-}free}$) versus liquidus depression, illustrating the reduction in heat flux relative to the sulfur-free end member due to lower crystallization temperatures. (b) The extended cooling duration $\Delta\tau$ as a function of liquidus depression for various graphite crust thickness (ranging from 1 m to 10,000 m). $\Delta\tau$ is defined as the difference in cooling time between the sulfur-bearing scenario (τ_C) and sulfur-free scenario (τ_0).

thousands of years. Specifically, for a 10,000-m-thick graphite crust, a liquidus depression of 200 °C extends the absolute cooling timescale by ~1117 years, compared to a baseline of ~9961 years in a S-free scenario. Ultimately, regardless of the graphite crust thickness, a 200 °C liquidus depression consistently yields a relative timescale extension of 11.2%.

To specifically investigate and isolate the role of sulfur on the dominant mode of solidification during the early, low-crystallinity stage of the magma ocean, we evaluated the critical crystal size (d_l) above which crystal settling and fractional crystallization theoretically occur (Solomatov, 2015; Fig. 9a).

$$d_l = \left(\frac{18\alpha F A_{mo} Z_{mo}\eta}{f g C_{p,\ mo}(\Delta\rho)^2 \phi V_{mo}}\right)^{1/2} \tag{15}$$

where α is the thermal expansion for silicate. F is the surface heat flux, Z_{mo} is the depth of MO, f is the hindered settling function, g is the gravitational acceleration on Mercury, $\Delta\rho$ is the density difference between crystal and liquid, ϕ is the crystal fraction, and V_{mo} is the volume of the magma ocean. The viscosity of the magma ocean (η) was calculated at the average MO temperature (T) using an Arrhenius-type relationship (Mouser et al., 2021; Fig. 9b):

$$\eta = \ln(A)\cdot exp\left(\frac{E + 0.5PV}{RT}\right) \tag{16}$$

where A is the pre-exponential factor, E is the activation energy, P is the pressure, V is the activation volume, R is the universal gas constant. The units and/or values of the variables in above equations could be seen in Supplementary Table S1.

Using these parameters, we obtained a critical crystal size of approximately 0.5 mm (Fig. 9a). The expected crystal sizes in Mercury's MO range from 0.5 to 10 mm, as inferred from terrestrial mantle xenoliths (Armienti and Tarquini, 2002). This is also consistent with the sizes observed in aubrite meteorites, which are widely considered the best available analogs for Mercury's mantle (Cartier and Wood, 2019). Because these estimated sizes meet or exceed this critical threshold (d_l), this physical condition intrinscially ensures that these crystals can overcome turbulen convective suspension and effectively settle. Therefore, fractional crystallization is viable mechanism for creating a chemically stratified mantle during the early liquid phase of the magma ocean (Saracino et al., 2025; Mouser et al., 2021)

Importantly, Eq. (15) indicates that the critical crystal size (d_l) is governed by the surface heat flux (F) and magma viscosity (η). Although sulfur compositionally decreases the viscosity of the Mercurian magma ocean (Mouser et al., 2021; Fig. 9b), any minor variations in η are entirely dwarfed by the orders-of-magnitude change in F dictated by the highly uncertain graphite crust thickness (Peplowski et al., 2016; Vander Kaaden and McCubbin, 2015). Ultimately, despite the effect of sulfur on magma viscosity, the physical viability of fractional crystallization is overwhelmingly dominated by the crust's thermal insulation. Regardless of the sulfur content, a sufficiently thick graphite crust ensures that crystals in the 0.5–10 mm range will effectively settle.

5. Conclusions

This experimental study shows and quantifies the critical role of sulfur in shaping the evolution of Mercury's mantle and magma ocean. Experimental results show that high sulfur concentrations (up to 6 wt.%) significantly depress silicate melt liquidus temperatures by as much as 200 °C, alter crystallization phase assemblages, decrease the mantle potential temperature required for melting, prolong magma ocean solidification timescales, and reduce critical crystal size. Together, these effects likely promoted fractional crystallization of distinct mineral phases, producing a stratified mantle. Subsequently partial melting of these heterogenous mantle layers would govern Mercury's internal dynamics and directly drive the generation of it compositionally diverse surface lavas.

Data availability: Data will be made available on request.

CRediT authorship contribution statement

Xiaofeng Lu: Writing – review & editing, Writing – original draft, Validation, Methodology, Investigation, Formal analysis, Data curation. **Olivier Namur:** Writing – review & editing, Writing – original draft, Validation, Investigation, Conceptualization. **Yongjiang Xu:** Writing – review & editing, Validation, Methodology, Investigation, Formal analysis. **Bernard Charlier:** Writing – review & editing, Validation, Methodology, Investigation, Conceptualization. **Yanhao Lin:** Writing – review & editing, Writing – original draft, Visualization, Validation, Supervision, Resources, Project administration, Methodology, Investigation, Funding acquisition, Conceptualization.

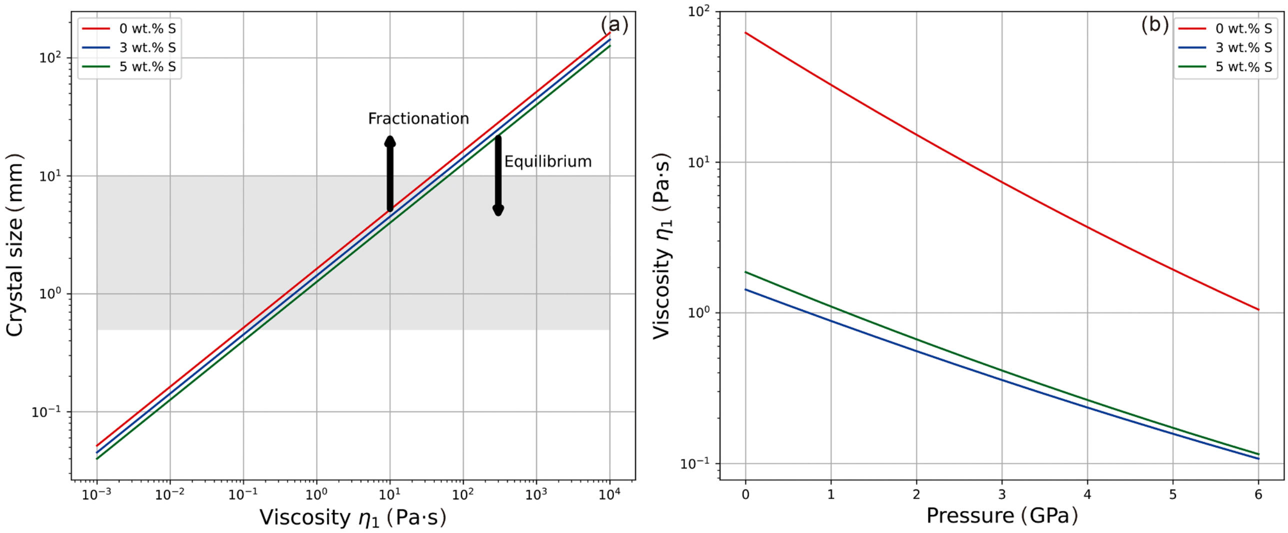

Fig. 9. Controls of sulfur content and viscosity on critical size during magma ocean crystallization. (a) Evolution of critical crystal size (d_ℓ) as a function of magma ocean viscosity. (b) Evolution of magma ocean viscosity as a function of bulk S content. The shaded grey band denotes the plausible crystal size range of 0.5–10 mm inferred from terrestrial mantle xenoliths (Armienti and Tarquini, 2002). The calculated viscosity ranges from 10^{-1} to 10^{2} Pa·s.

Declaration of competing interest

The authors declare that they have no known competing financial interests or personal relationships that could have appeared to influence the work reported in this paper.

Acknowledgements

We thank Shuang Xu for technical assistance on electron microprobe analyses. We also thank Nicholas Dygert and an anonymous reviewer for their constructive comments on this mannuscript. This research was supported by a grant from the National Key Research and Development Program of China (Grant No. 2024YFF0807500) and the National Natural Science Foundation of China awarded to Y.L. (42250105), and Center for High Pressure Science and Technology Advanced Research is supported by the National Science Foundation of China (Grants U1530402 and U1930401). B.C. is a Research Associate of the Belgian Fund for Scientific Research-FNRS and acknowledges funding from the ESA PRODEX Program (Grant 4000142722). O.N. acknowledges support from the European Research Council (ERC) under the European Union's Horizon (grant agreement no. 101125126; IronHeart).

Supplementary materials

Supplementary material associated with this article can be found, in the online version, at doi:10.1016/j.epsl.2026.120123.

Data availability

Data will be made available on request.

References

Almeev, R.R., Holtz, F., Koepke, J., Parat, F., 2012. Experimental calibration of the effect of H_2O on plagioclase crystallization in basaltic melt at 200 MPa. Am. Mineral. 97, 1234–1240. https://doi.org/10.2138/am.2012.4100.

Almeev, R.R., Holtz, F., Koepke, J., Parat, F., Botcharnikov, R.E., 2007. The effect of H_2O on olivine crystallization in MORB: experimental calibration at 200 MPa. Am. Mineral. 92, 670–674. https://doi.org/10.2138/am.2007.2484.

Andersen, O., 1915. The system anorthite-forsterite-silica. Am. J. Sci.. s4-39, 407–454. https://doi.org/10.2475/ajs.s4-39.232.407.

Anzures, B.A., Parman, S.W., Milliken, R.E., Namur, O., Cartier, C., McCubbin, F.M., Vander Kaaden, K.E., Prissel, K., Iacovino, K., Lanzirotti, A., Newville, M., 2025. An oxygen fugacity-temperature-pressure-composition model for sulfide speciation in Mercurian magmas. Geochim. Cosmochim. Acta 388, 61–77. https://doi.org/10.1016/j.gca.2024.11.012.

Anzures, B.A., Parman, S.W., Milliken, R.E., Namur, O., Cartier, C., Wang, S., 2020. Effect of sulfur speciation on chemical and physical properties of very reduced mercurian melts. Geochim. Cosmochim. Acta 286, 1–18. https://doi.org/10.1016/j.gca.2020.07.024.

Armienti, P., Tarquini, S., 2002. Power law olivine crystal size distributions in lithospheric mantle xenoliths. Lithos 65, 273–285. https://doi.org/10.1016/S0024-4937(02)00195-0.

Berthet, S., Malavergne, V., Righter, K., 2009. Melting of the Indarch meteorite (EH4 chondrite) at 1GPa and variable oxygen fugacity: implications for early planetary differentiation processes. Geochim. Cosmochim. Acta 73, 6402–6420. https://doi.org/10.1016/j.gca.2009.07.030.

Botcharnikov, R.E., Almeev, R.R., Koepke, J., Holtz, F., 2008. Phase relations and liquid lines of descent in hydrous ferrobasalt-implications for the skaergaard intrusion and columbia river flood basalts. J. Petrol. 49, 1687–1727. https://doi.org/10.1093/petrology/egn043.

Boujibar, A., Righter, K., Fontaine, E., Collinet, M., Lambart, S., Nittler, L.R., Pando, K. M., 2025. A Pyroxenite mantle on Mercury? Experimental insights from enstatite chondrite melting at pressures up to 5 GPa. Icarus 437, 116602. https://doi.org/10.1016/j.icarus.2025.116602.

Cartier, C., Hammouda, T., Doucelance, R., Boyet, M., Devidal, J.-L., Moine, B., 2014. Experimental study of trace element partitioning between enstatite and melt in enstatite chondrites at low oxygen fugacities and 5 GPa. Geochim. Cosmochim. Acta 130, 167–187. https://doi.org/10.1016/j.gca.2014.01.002.

Cartier, C., Wood, B.J., 2019. The role of reducing conditions in building Mercury. Elements 15, 39–45. https://doi.org/10.2138/gselements.15.1.39.

Chabot, N.L., Wollack, E.A., Klima, R.L., Minitti, M.E., 2014. Experimental constraints on Mercury's core composition. Earth. Planet. Sci. Lett. 390, 199–208. https://doi.org/10.1016/j.epsl.2014.01.004.

Filiberto, J., Treiman, A.H., 2009. The effect of chlorine on the liquidus of basalt: first results and implications for basalt genesis on Mars and Earth. Chem. Geol. 263, 60–68. https://doi.org/10.1016/j.chemgeo.2008.08.025.

Filiberto, J., Wood, J., Dasgupta, R., Shimizu, N., Le, L., Treiman, A.H., 2012. Effect of fluorine on near-liquidus phase equilibria of an Fe-Mg rich basalt. Chem. Geol. 312-313, 118–126. https://doi.org/10.1016/j.chemgeo.2012.04.015.

Fogel, R.A., 2005. Aubrite basalt vitrophyres: the missing basaltic component and high-sulfur silicate melts. Geochim. Cosmochim. Acta 69, 1633–1648. https://doi.org/10.1016/j.gca.2003.11.032.

Goossens, S., Renaud, J.P., Henning, W.G., Mazarico, E., Bertone, S., Genova, A., 2022. Evaluation of recent measurements of Mercury's moments of inertia and tides using a comprehensive Markov Chain Monte Carlo method. Planet. Sci. J. 3, 37. https://doi.org/10.3847/PSJ/ac4bb8.

Green, E.C., Holland, T.J., Powell, R., Weller, O.M., Riel, N., 2025. Corrigendum to: melting of peridotites through to granites: a simple thermodynamic model in the system kncfmashtocr, and, a thermodynamic model for the subsolidus evolution and melting of peridotite. J. Petrol. 66 (1), egae079. https://doi.org/10.1093/petrology/egae079.

Hauck, S.A., Margot, J.L., Solomon, S.C., Phillips, R.J., Johnson, C.L., Lemoine, F.G., Mazarico, E., McCoy, T.J., Padovan, S., Peale, S.J., Perry, M.E., Smith, D.E., Zuber, M.T., 2013. The curious case of Mercury's internal structure. J. Geophys. Res., Planets 118, 1204–1220. https://doi.org/10.1002/jgre.20091.

Hirschmann, M.M., Tenner, T., Aubaud, C., Withers, A.C., 2009. Dehydration melting of nominally anhydrous mantle: the primacy of partitioning. Phys. Earth Planet. Inter. 176, 54–68. https://doi.org/10.1016/j.pepi.2009.04.001.

Holland, T.J.B., Green, E.C.R., Powell, R., 2018. Melting of peridotites through to granites: a simple thermodynamic model in the system KNCFMASHTOCr. J. Petrol. 59, 881–900. https://doi.org/10.1093/petrology/egy048.

Huebner, J.S., 1971. Buffering techniques for hydrostatic systems at elevated pressures. In: Ulmer, G.C. (Ed.), Research Techniques for High Pressure and High Temperature, pp. 123–177. https://doi.org/10.1007/978-3-642-88097-1_5.

Jarosewich, E., 1990. Chemical analyses of meteorites: a compilation of stony and iron meteorite analyses. Meteoritics 25, 323–337. https://doi.org/10.1111/j.1945-5100.1990.tb00717.x.

Jugo, P.J., Wilke, M., Botcharnikov, R.E., 2010. Sulfur K-edge XANES analysis of natural and synthetic basaltic glasses: implications for S speciation and S content as function of oxygen fugacity. Geochim. Cosmochim. Acta 74, 5926–5938. https://doi.org/10.1016/j.gca.2010.07.022.

Katz, R.F., Spiegelman, M., Langmuir, C.H., 2003. A new parameterization of hydrous mantle melting. Geochem. Geophys. Geosystems 4, 1073. https://doi.org/10.1029/2002GC000433.

Kilburn, M.R., Wood, B.J., 1997. Metal-silicate partitioning and the incompatibility of S and Si during core formation. Earth. Planet. Sci. Lett. 152, 139–148. https://doi.org/10.1016/S0012-821X(97)00125-8.

Knibbe, J.S., Rivoldini, A., Luginbuhl, S.M., Namur, O., Charlier, B., Mezouar, M., Sifre, D., Berndt, J., Kono, Y., Neuville, D.R., Westrenen van, W., Hoolst, T.V., 2021. Mercury's interior structure constrained by density and P-wave velocity measurements of liquid Fe-Si-C alloys. J. Geophys. Res.: Planets 126, e2020JE006651. https://doi.org/10.1029/2020JE006651.

Koch, L., Almeev, R.R., Linsler, S.A., Marxer, F., Holtz, F., 2025. The effect of H_2O on the crystallization of orthopyroxene in a high-Mg andesitic melt. Am. Mineral. https://doi.org/10.2138/am-2024-9593.

Kojitani, H., Akaogi, M., 1997. Melting enthalpies of mantle peridotite: calorimetric determinations in the system CaO-MgO-Al_2O_3-SiO_2 and application to magma generation. Earth. Planet. Sci. Lett. 153, 209–222. https://doi.org/10.1016/S0012-821X(97)00186-6.

Lin, Y., Ishii, T., van Westrenen, W., Katsura, T., Mao, H.-K., 2024. Melting at the base of a terrestrial magma ocean controlled by oxygen fugacity. Nat. Geosci. 17, 803–808. https://doi.org/10.1038/s41561-024-01495-1.

Lin, Y., Tronche, E.J., Steenstra, E.S., van Westrenen, W., 2017. Evidence for an early wet Moon from experimental crystallization of the lunar magma ocean. Nat. Geosci. 10, 14–18. https://doi.org/10.1038/ngeo2845.

Lin, Y., van Westrenen, W., 2021. Oxygen as a catalyst in the Earth's interior? Natl. Sci. Rev. 8, nwab009. https://doi.org/10.1093/nsr/nwab009.

Lin, Y., van Westrenen, W., Mao, H.-K., 2021. Oxygen controls on magmatism in rocky exoplanets. Proc. Natl. Acad. Sci. U.S.A. 118, e2110427118. https://doi.org/10.1073/pnas.2110427118.

Liu, T.-C., Presnall, D.C., 1990. Liquidus phase relationships on the join anorthite-forsterite-quartz at 20 kbar with applications to basalt petrogenesis and igneous sapphirine. Contrib. Mineral. Petrol. 104, 735–742. https://doi.org/10.1007/BF01167290.

Lodders, K., Fegley, B.J.R, 1998. The Planetary Scientist's Companion. Oxford University Press.

Longhi, J., 1987. Liquidus equilibria and solid solution in the system $CaAl_2Si_2O_8$-Mg_2SiO_4-$CaSiO_3$-SiO_2 at low pressure. Am. J. Sci. 287, 265–331. https://doi.org/10.2475/ajs.287.4.265.

Malavergne, V., Cordier, P., Righter, K., Brunet, F., Zanda, B., Addad, A., Smith, T., Bureau, H., Surblé, S., Raepsaet, C., Charon, E., Hewins, R.H., 2014. How Mercury can be the most reduced terrestrial planet and still store iron in its mantle. Earth. Planet. Sci. Lett. 394, 186–197. https://doi.org/10.1016/j.epsl.2014.03.028.

Malavergne, V., Toplis, M.J., Berthet, S., Jones, J., 2010. Highly reducing conditions during core formation on Mercury: implications for internal structure and the origin of a magnetic field. Icarus 206, 199–209. https://doi.org/10.1016/j.epsl.2024.118812.

Margot, J.L., Hauck, S.A., Mazarico, E., Padovan, S., Peale, S.J., 2018. Mercury's internal structure. in: Mercury. View MSSENGER 85–113. https://doi.org/10.1017/9781316650684.005.

McCubbin, F.M., Riner, M.A., Vander Kaaden, K.E., Burkemper, L.K., 2012. Is Mercury a volatile-rich planet? Geophys. Res. Lett. 39. https://doi.org/10.1029/2012GL051711.

McKenzie, D., Bickle, M.J., 1988. The volume and composition of melt generated by extension of the lithosphere. J. Petrol. 29, 625–679. https://doi.org/10.1093/petrology/29.3.625.

Médard, E., Grove, T.L., 2008. The effect of H_2O on the olivine liquidus of basaltic melts: experiments and thermodynamic models. Contrib. Mineral. Petrol. 155, 417–432. https://doi.org/10.1007/s00410-007-0250-4.

Métrich, N., Berry, A.J., O'Neill, H.S.T.C., Susini, J., 2009. The oxidation state of sulfur in synthetic and natural glasses determined by X-ray absorption spectroscopy. Geochim. Cosmochim. Acta 73, 2382–2399. https://doi.org/10.1016/j.gca.2009.01.025.

Morard, G., Katsura, T., 2010. Pressure-temperature cartography of Fe-S-Si immiscible system. Geochim. Cosmochim. Acta 74, 3659–3667. https://doi.org/10.1016/j.gca.2010.03.025.

Mouser, M.D., Dygert, N., 2023. On the potential for cumulate mantle overturn in Mercury. J. Geophys. Res.: Planets 128, e2023JE007739. https://doi.org/10.1029/2023JE007739.

Mouser, M.D., Dygert, N., Anzures, B.A., Grambling, N.L., Hrubiak, R., Kono, Y., Shen, G., Parman, S.W., 2021. Experimental investigation of Mercury's magma ocean viscosity: implications for the formation of Mercury's cumulate mantle, Its subsequent dynamic evolution, and crustal petrogenesis. J. Geophys. Res.: Planets 126, e2021JE006946. https://doi.org/10.1029/2021JE006946.

Namur, O., Charlier, B., Holtz, F., Cartier, C., McCammon, C., 2016a. Sulfur solubility in reduced mafic silicate melts: implications for the speciation and distribution of sulfur on Mercury. Earth. Planet. Sci. Lett. 448, 102–114. https://doi.org/10.1016/j.epsl.2016.05.024.

Namur, O., Collinet, M., Charlier, B., Grove, T.L., Holtz, F., McCammon, C., 2016b. Melting processes and mantle sources of lavas on Mercury. Earth. Planet. Sci. Lett. 439, 117–128. https://doi.org/10.1016/j.epsl.2016.01.030.

Nittler, L.R., Chabot, N.L., Grove, T.L., Peplowski, P.N., 2018. The Chemical Composition of Mercury. Mercury: The View After MESSENGER Ch 2. Cambridge University Press, Cambridge. https://doi.org/10.1017/9781316650684.003.

Peplowski, P.N., Klima, R.L., Lawrence, D.J., Ernst, C.M., Denevi, B.W., Frank, E.A., Goldsten, J.O., Murchie, S.L., Nittler, L.R., Solomon, S.C., 2016. Remote sensing evidence for an ancient carbon-bearing crust on mercury. Nat. Geosci. 9, 273–276. https://doi.org/10.1038/ngeo2669.

Pommier, A., Tauber, M.J., Pirotte, H., Cody, G.D., Steele, A., Bullock, E.S., Charlier, B., Mysen, B.O., 2023. Experimental investigation of the bonding of sulfur in highly reduced silicate glasses and melts. Geochim. Cosmochim. Acta 363, 114–128. https://doi.org/10.1016/j.gca.2023.10.027.

Prockter, L.M., Ernst, C.M., Denevi, B.W., Chapman, C.R., Head, J.W., Fassett, C.I., Merline, W.J., Solomon, S.C., Watters, T.R., Strom, R.G., Cremonese, G., Marchi, S., Massironi, M., 2010. Evidence for young volcanism on Mercury from the third MESSENGER flyby. Science 329, 668–671. https://doi.org/10.1126/science.1188186.

Riel, N., Kaus, B.J.P., Green, E.C.R., Berlie, N., 2022. MAGEMin, an efficient gibbs energy minimizer: application to igneous systems. Geochem. Geophys. Geosystems 23, e2022GC010427. https://doi.org/10.1029/2022GC010427.

Robie, R.A., Hemingway, B.S., 1995. Thermodynamic properties of minerals and related substances at 298.15 K and 1 Bar (10^5 Pascals) pressure and at higher temperatures. Bulletin. https://doi.org/10.3133/b2131.

Saracino, F., Charlier, B., Zhang, Y., Lécaille, M., Lin, Y., Namur, O., 2025. The role of sulfur on the liquidus temperature and olivine-orthopyroxene equilibria in highly reduced magmas. Chem. Geol. 683, 122777. https://doi.org/10.1016/j.chemgeo.2025.122777.

Sen, G., Presnall, D.C., 1984. Liquidus phase relationships on the join anorthite-forsterite-quartz at 10 kbar with applications to basalt petrogenesis. Contrib. Mineral. Petrol. 85, 404–408. https://doi.org/10.1007/BF01150296.

Sisson, T.W., Grove, T.L., 1993. Experimental investigations of the role of H_2O in calc-alkaline differentiation and subduction zone magmatism. Contrib. Mineral. Petrol. 113, 143–166. https://doi.org/10.1007/BF00283225.

Solomatov, V.S., 2015. WITHDRAWN: the terrestrial magma ocean hypothesis. Gondwana Res. https://doi.org/10.1016/j.gr.2015.07.018.

Steenstra, E.S., Seegers, A.X., Eising, J., Tomassen, B.G.J., Webers, F.P.F., Berndt, J., Klemme, S., Matveev, S., Van Westrenen, W., 2018. Evidence for a sulfur-undersaturated lunar interior from the solubility of sulfur in lunar melts and sulfide-silicate partitioning of siderophile elements. Geochim. Cosmochim. Acta 231, 130–156. https://doi.org/10.1016/j.gca.2020.07.002.

Steenstra, E.S., Seegers, A.X., Putter, R., Berndt, J., Klemme, S., Matveev, S., Bullock, E. S., van Westrenen, W., 2020. Metal-silicate partitioning systematics of siderophile elements at reducing conditions: a new experimental database. Icarus 335, 113391. https://doi.org/10.1016/j.gca.2018.04.008.

Vander Kaaden, K.E., McCubbin, F.M., 2015. Exotic crust formation on Mercury: consequences of shallow, FeO-poor mantle. J. Geophys. Res. Planets. 120, 195–209. https://doi.org/10.1002/2014JE004733.

Weider, S.Z., Nittler, L.R., Starr, R.D., Crapster-Pregont, E.J., Peplowski, P.N., Denevi, B. W., Head, J.W., Byrne, P.K., Hauck, S.A., Ebel, D.S., Solomon, S.C., 2015. Evidence for geochemical terranes on Mercury: global mapping of major elements with MESSENGER's X-Ray Spectrometer. Earth. Planet. Sci. Lett. 416, 109–120. https://doi.org/10.1016/j.epsl.2015.01.023.

Weider, S.Z., Nittler, L.R., Starr, R.D., McCoy, T.J., Solomon, S.C., 2014. Variations in the abundance of iron on Mercury's surface from MESSENGER X-Ray Spectrometer observations. Icarus 235, 170–186. https://doi.org/10.1016/j.icarus.2014.03.002.

Wu, P., Xu, Y., Lin, Y., 2024. A novel rapid cooling assembly design in a high-pressure cubic press apparatus. Matter Radiat. Extrem. 9, 027402. https://doi.org/10.1063/5.0176025.

Xu, Q., Gao, S., van Westrenen, W., Gréaux, S., Kono, Y., Wu, P., Shang, S., Xiang, H., Kakizawa, S., Tsujino, N., Higo, Y., Lin, Y., 2026a. Reactive formation of magnesiowüstite at the lunar core-mantle boundary. Nat. Commun. 17, 3705. https://doi.org/10.1038/s41467-026-71701-8.

Xu, R., Xiao, Z., Wang, Y., Cui, J., 2024a. Less than one weight percent of graphite on the surface of Mercury. Nat. Astron. 8, 280–289. https://doi.org/10.1038/s41550-023-02169-5.

Xu, Y., Lin, Y., Wu, P., Namur, O., Zhang, Y., Charlier, B., 2024b. A diamond-bearing core-mantle boundary on Mercury. Nat. Commun. 15, 5061. https://doi.org/10.1038/s41467-024-49305-x.

Xu, Y., Wu, P., Shang, S., Wang, X., Li, T., Gao, S., Lv, S., Cheng, H., Xu, Q., Lei, S., Feng, J., Zhao, L., van Westrenen, W., Ishii, T., Chen, B., Su, L., Ding, Y., Yang, W., Mao, H.-K., Lin, Y., 2026. Pressure calibrations of high-pressure large-volume presses at. HPSTAR. Matter Radiat. Extremes 11 (1). https://doi.org/10.1063/5.0289378.

Zeng, Q., Nekvasil, H., Grey, C.P., 1999. Proton environments in hydrous aluminosilicate glasses: A ^{1}H MAS, ^{1}H/^{27}Al, and ^{1}H/^{23}Na TRAPDOR NMR Study. J. Phys. Chem. B 103, 7406–7415. https://doi.org/10.1021/jp990726l.

Zhang, Y., Dasgupta, R., 2026. The effects of sulfur on near-liquidus phase relations of highly reduced basaltic melts with implications for magmatism in Mercury. Geochim. Cosmochim. Acta 420, 399–417. https://doi.org/10.1016/j.gca.2026.02.034.

Zhang, Z., Pan, J.S., Zhang, J., Tok, E.S., 2010. Kinetics of Ge diffusion, desorption and pit formation dynamics during annealing of $Si_{0.8}Ge_{0.2}$/Si (001) virtual substrates. Phys. Chem. Chem. Phys. 12, 7171–7183. https://doi.org/10.1039/B927274G.

Zolotov, M.Y.U., Sprague, A.L., Hauck II, S.A., Nittler, L.R., Solomon, S.C., Weider, S.Z., 2013. The redox state, FeO content, and origin of sulfur-rich magmas on Mercury. J. Geophys. Res.: Planets 118, 138–146. https://doi.org/10.1029/2012JE004274.